

FORMALDEHYDE ANTI-INVERSION AT $z = 0.68$ IN THE GRAVITATIONAL LENS B0218+357

BENJAMIN ZEIGER^{1,2} & JEREMY DARLING^{1,3,4}
The Astrophysical Journal **709** (2010) 386

ABSTRACT

We report new observations of the $1_{10}-1_{11}$ (6 cm) and $2_{11}-2_{12}$ (2 cm) transitions of ortho-formaldehyde (o-H₂CO) in absorption at $z = 0.68466$ toward the gravitational lens system B0218+357. Radiative transfer modeling indicates that both transitions are anti-inverted relative to the 4.6 K cosmic microwave background (CMB), regardless of the source covering factor, with excitation temperatures of ~ 1 K and 1.5–2 K for the $1_{10}-1_{11}$ and $2_{11}-2_{12}$ lines, respectively. Using these observations and a large velocity gradient radiative transfer model that assumes a gradient of $1 \text{ km s}^{-1} \text{ pc}^{-1}$, we obtain a molecular hydrogen number density of $2 \times 10^3 \text{ cm}^{-3} < n(\text{H}_2) < 1 \times 10^4 \text{ cm}^{-3}$ and a column density of $2.5 \times 10^{13} \text{ cm}^{-2} < N(\text{o-H}_2\text{CO}) < 8.9 \times 10^{13} \text{ cm}^{-2}$, where the allowed ranges conservatively include the range of possible source covering factors in both lines. The measurements suggest that H₂CO excitation in the absorbing clouds in the B0218+357 lens is analogous to that in Galactic molecular clouds: it would show H₂CO absorption against the CMB if it were not illuminated by the background quasar or if it were viewed from another direction.

Subject headings: galaxies: individual (B0218+357) — galaxies: ISM — radiation mechanisms: non-thermal — radio lines: galaxies — quasars: absorption lines

1. INTRODUCTION

Formaldehyde (H₂CO) centimeter transitions have been observed with excitation temperatures less than the temperature of the cosmic microwave background ($T_{\text{ex}} < T_{\text{CMB}}$) in the Milky Way (Palmer et al. 1969). The “anti-inversion,” or non-thermal absorption, is pumped by collisions, coupling H₂CO excitation to the number density $n(\text{H}_2)$ of molecular hydrogen even at kinetic temperatures as low as ~ 10 K (Townes & Cheung 1969; Evans et al. 1975; Garrison et al. 1975). Thus, H₂CO provides a density and temperature diagnostic for molecular gas (Mühle, Seaquist, & Henkel 2007; Mangum et al. 2008), and it often produces detectable lines before dense molecular clouds begin to form stars and warm sufficiently to emit lines from the usual molecular tracers such as CO and HCO⁺.

The rotation states of H₂CO are defined by the three quantum numbers J_{K_a, K_c} (total angular momentum and the angular momenta about the axes with the smallest and largest moments of inertia, respectively). The lower energy transitions for $K_a < 2$ are shown in Figure 1. The spin symmetry of the hydrogen nuclei defines the ortho ($K_a = \text{odd}$) and para ($K_a = \text{even}$) states. Since the spin symmetry is about the a axis, which is aligned with the electric dipole along the C–O double bond and thus unchanged by dipole interactions, the mean transition time from o-H₂CO to p-H₂CO states (or vice versa) is longer than the mean life of the molecule, and the ortho/para ratio preserves information about the dominant formation channel: a ratio of unity indicates catalysis on the surface of cold ($T_{\text{kin}} \lesssim 15$ K) dust grains, while a ratio of 3 indicates gas-phase formation (Kahane et al. 1984; Dickens & Irvine 1999).

The most commonly detected o-H₂CO lines are the $\Delta J = 0$,

$\Delta K_c = \pm 1$ “ K -doublet” $1_{10}-1_{11}$ 4.8 GHz (6 cm) and $2_{11}-2_{12}$ 14.5 GHz (2 cm) centimeter transitions and the $\Delta J = \pm 1$, $\Delta K_c = \pm 1$ millimeter transitions connecting the $J = 1$ states to the $J = 2$ states at 140.8 and 150.5 GHz ($2_{12}-1_{11}$ and $2_{11}-1_{10}$, respectively). The coupling of the centimeter and millimeter transitions allows the K -doublet transitions to be driven significantly out of local thermodynamic equilibrium (LTE) and makes H₂CO an *in situ* probe of conditions in molecular clouds. The relative excitation of K -doublets is a powerful densitometer (Mangum et al. 2008), while the relative excitation of millimeter lines is a molecular thermometer (Mühle, Seaquist, & Henkel 2007). The $1_{10}-1_{11}$ and $2_{11}-2_{12}$ transitions have both been observed with population anti-inversions, causing stimulated absorption of the CMB, and the $1_{10}-1_{11}$ transition has been observed as a maser (Haar & Pelling 1974; Evans et al. 1975; Araya et al. 2008).

We report observations of the $1_{10}-1_{11}$ and $2_{11}-2_{12}$ transitions in absorption toward B0218+357, a gravitational lens system with two images separated by $0''.33$. The lens lies at a redshift of $z = 0.68466(4)$ (Browne et al. 1993), while the background quasar is at $z = 0.944(2)$ (Cohen et al. 2003). At low frequencies, the “gravitational lens with the smallest separation” of its images also displays the smallest known Einstein ring, with a diameter of $0''.335$ (Patnaik et al. 1993). The two images, dubbed A and B in order of radio brightness, display significantly different absorption characteristics, with B unobscured while A shows strong molecular absorption lines and is heavily obscured by dust in optical observations (Wiklind & Combes 1995; Grundahl & Hjorth 1995). Both A and B show the background source to have a core-jet morphology.

Many molecules have been observed at the redshift of the lens in absorption against the strong continuum of image A, including CO, HCO⁺, HCN, H₂O, NH₃, OH, and H₂CO; typical line widths are $10\text{--}15 \text{ km s}^{-1}$ (Wiklind & Combes 1995; Combes & Wiklind 1997; Henkel et al. 2005; Kanekar et al. 2003; Menten & Reid 1996). H I observations indicate the lensing galaxy to be gas-rich, with a column density

¹ Center for Astrophysics and Space Astronomy, Department of Astrophysical and Planetary Sciences, University of Colorado, 389 UCB, Boulder, CO 80309-0389, USA

² benjamin.zeiger@colorado.edu

³ NASA Lunar Science Institute, NASA Ames Research Center, Moffett Field, CA, USA

⁴ jdarling@colorado.edu

Table 1
Journal of o-H₂CO Observations Toward B0218+357

Telescope	Receiver	UT Date	Transition	ν_o (GHz)	ν_{obs} (GHz)	t_{int} (s)	Δv^a (km s ⁻¹)	rms (mJy)
Arecibo	S-low	2004 Aug 3–4	1 ₁₀ –1 ₁₁	4.829660(1)	2.8668455(6)	3600 ^b	1.3	0.8
GBT	X	2006 Apr 26	2 ₁₁ –2 ₁₂	14.488479(1)	8.6002392(6)	3280	2.1	1.1

^a Δv is the rest-frame spectral velocity resolution of the final, smoothed spectrum.

^b Two 1800 s sessions from consecutive days were combined for the final spectrum.

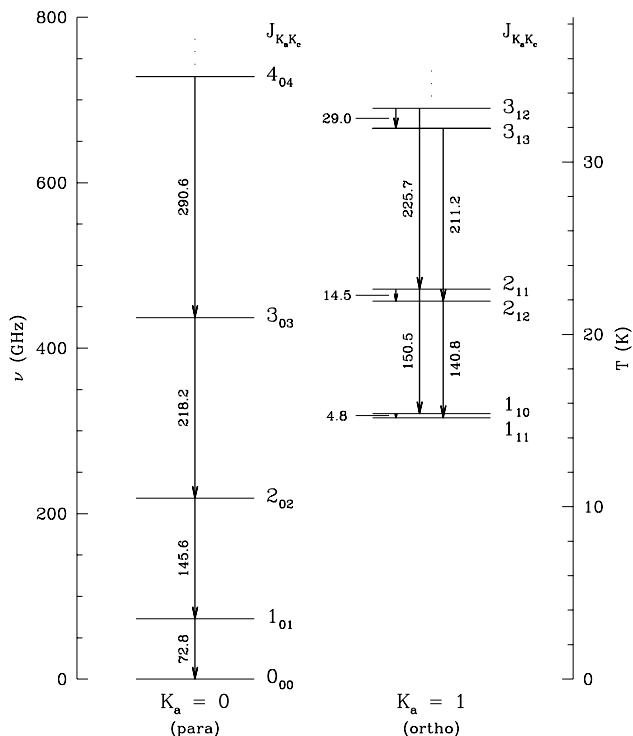


Figure 1. Formaldehyde (H₂CO) energy level diagram showing only the lower levels and $K_a < 2$. The indicated transitions are in GHz.

$N(\text{H I}) = 4 \times 10^{18} (T_s/f) \text{ cm}^{-2}$ across a line width (FWHM) of 43 km s⁻¹, where T_s is the spin temperature and f is the H I covering factor (Carilli et al. 1993). Four spectrally resolved absorption components can be identified in front of image A in high-resolution interferometric HCO⁺ observations (Muller et al. 2007).

H₂CO was first observed in B0218+357 by Menten & Reid (1996) in the 2₁₁–2₁₂ transition in absorption. Jethava et al. (2007) followed these observations with a six-line study of H₂CO in B0218+357, adding observations of the lowest two $\Delta J = 1$ rotational transitions of both the ortho and the para species, as well as the 1₁₀–1₁₁ transition of o-H₂CO. Using the 55 K kinetic temperature derived from NH₃ observations (Henkel et al. 2005) and a large velocity gradient (LVG) model to determine the non-thermal H₂CO excitation due to collisions with H₂, Jethava et al. (2007) determined a spatial number density of $n(\text{H}_2) < 10^3 \text{ cm}^{-3}$ and a column density of $N(\text{H}_2\text{CO}) \approx 5.2 \times 10^{13} \text{ cm}^{-2}$ (no confidence interval is reported) in the strongest absorption component, with a weaker component adding $\sim 15\%$ to the column density. They measured an o-H₂CO/p-H₂CO ratio of 2.0–3.0 with a best fit of 2.8, giving $N(\text{o-H}_2\text{CO}) = 3.8 \times 10^{13} \text{ cm}^{-2}$. They do not address the issue of H₂CO excitation temperatures, which are of

interest because anti-inversion of the lines would imply that the gas in the B0218+357 lens would be visible in absorption against the CMB even without a background quasar to illuminate it. Obtaining excitation temperatures of H₂CO lines in B0218+357 will help to set H₂CO observability conditions in non-lensing (or otherwise unilluminated) galaxies.

The Mangum et al. (2008) survey of local galaxies demonstrates the feasibility of determining both $n(\text{H}_2)$ and $N(\text{o-H}_2\text{CO})$ strictly from the 1₁₀–1₁₁ and 2₁₁–2₁₂ transitions. The relative strengths of the transitions are set by the degree of collisional excitation, giving a precise densitometer that, in turn, yields the excitation temperatures of the transitions. In our analysis, we use the two-line densitometry method with new data, including 1₁₀–1₁₁ observations of higher spectral resolution and signal to noise ratio than that obtained by Jethava et al. (2007) and 2₁₁–2₁₂ observations with lower signal to noise (4.7 versus 8.8) but comparable resolution to those of Menten & Reid (1996). Our analysis, while also yielding $N(\text{o-H}_2\text{CO})$ and $n(\text{H}_2)$ from an exhaustive search of the density space with our LVG model, focuses on line excitation temperatures in B0218+357 to show that the o-H₂CO observed in absorption is anti-inverted relative to the 4.6 K T_{CMB} at $z = 0.68$, making it analogous to Galactic molecular clouds that show anti-inversion of the K -doublet transitions and thus CMB absorption.

In Section 2, we describe our observational and data reduction procedures used to acquire and reduce the new high resolution spectra of the 1₁₀–1₁₁ and 2₁₁–2₁₂ o-H₂CO transitions in B0218+357. The properties of both lines are reported in Section 3, and we use those results to determine $n(\text{H}_2)$, $N(\text{o-H}_2\text{CO})$, and line excitation temperatures in Section 4. We show that the absorbing clouds in B0218+357 are analogous to Galactic molecular clouds that show anti-inversion of o-H₂CO centimeter lines relative to the $z = 0$ T_{CMB}, and that the anti-inversion of K -doublet transitions persists up to the 6₁₅–6₁₆ (101 GHz rest) transition (Section 5). The consequences of our results are discussed in Section 6.

2. OBSERVATIONS AND DATA REDUCTION

2.1. Arecibo Telescope: 1₁₀–1₁₁ Line

We observed the 1₁₀–1₁₁ 4.829660(1) GHz transition⁵ of o-H₂CO, redshifted to 2.8668455(6) GHz, toward B0218+357 at the Arecibo radio telescope⁶ in August 2004 (Table 1). Observations were conducted with a 6.25 MHz band centered on the redshifted line, using 5 minute position-switched scans with a calibration diode fired after each position-switched pair and spectral records recorded every 6 s. Total integration time was 3600 s. The autocorrelation spectrometer used

⁵ All line frequencies are from the JPL molecular line database (Pickett et al. 1998).

⁶ The Arecibo Observatory is part of the National Astronomy and Ionosphere Center, which is operated by Cornell University under a cooperative agreement with the National Science Foundation.

Table 2
Measured and Calculated Formaldehyde Line Properties

Transition	ν_o (GHz)	Compt	$v_{\text{obs}} - v_{\text{sys}}$ (km s ⁻¹)	Depth (mJy)	FWHM (km s ⁻¹)	τ_{app}	$\int \tau_{\text{app}} dv$ (km s ⁻¹)
1 ₁₀ -1 ₁₁	4.829660(1)	1	+3.7(0.4)	9.6(0.4)	12.3(0.6)	0.017(1)	0.239(8)
		2	-9.8(2.4)	1.8(0.3)	14.2(4.0)		
		Total	+3.4(0.4)	10.8(0.8)	12.6(0.6)		
2 ₁₁ -2 ₁₂	14.488479(1)	1	+4.2(0.8)	5.2(1.1)	8.5(1.5)	0.008(2)	0.083(10)

Note. — $v_{\text{obs}} - v_{\text{sys}}$ is the *rest-frame* centroid velocity offset from the assumed systemic redshift, $z = 0.68466$, FWHM is the rest-frame line width, and τ_{app} is the maximum apparent optical depth in the line, assuming a covering factor of unity and a continuum in image A of 650 ± 16 and 663 ± 22 mJy in the 1₁₀-1₁₁ and 2₁₁-2₁₂ lines, respectively (Section 3). Uncertainties are strictly statistical uncertainties from the spectra and do not reflect the systematic uncertainties associated with flux calibration or the radio continuum determinations. Reported quantities for the 1₁₀-1₁₁ “Total” and 2₁₁-2₁₂ lines are measured directly from the data and are not dependent on profile fitting; the individual components of the 1₁₀-1₁₁ line are from Gaussian fits.

nine-level sampling in two (subsequently averaged) polarizations. Bandpasses were divided into 1024 channels and Hanning smoothed to 512 channels. Rest-frame velocity resolution was 1.3 km s⁻¹ (see Table 1). The observed band was interference-free in the vicinity of the observed line.

Records were individually calibrated and bandpasses were flattened using the calibration diode and the corresponding off-source records. Records and polarizations were subsequently averaged, and a polynomial baseline with variations much larger than the line was fit to and subtracted from the spectrum. Systematic flux calibration errors in these data are of order 10%. All data reduction was performed in the Astronomical Information Processing System++, AIPS++.⁷ Arecibo spectra often show spectral standing waves due to resonances of the strong continuum flux densities within the telescope superstructure. The line width was significantly less than the size of the standing wave features, so the spectrum was not significantly affected.

2.2. Green Bank Telescope: 2₁₁-2₁₂ Line

We observed the 2₁₁-2₁₂ 14.488479(1) GHz transition of H₂CO, redshifted to 8.6002392(6) GHz, toward B0218+357 with the Green Bank Telescope⁸ (GBT) on 2006 April 26 (Table 1). Observations were conducted with a 50 MHz bandpass centered on the redshifted line in 5 minute position-switched scans with spectral data recorded every 3 s and a winking calibration diode firing during every other record. The total on-source integration time was 3280 s. The autocorrelation spectrometer used nine-level sampling in two (subsequently averaged) linear polarizations. Bandpasses were divided into 16384 channels, Hanning smoothed to 8192 independent channels, and 10-channel Gaussian smoothed to a rest-frame velocity resolution of 2.1 km s⁻¹. Records were individually calibrated and bandpasses were flattened using the calibration diode and the corresponding off-source records. The individual spectra were interference-free and fairly flat, but the DC levels of the individual scans showed significant fluctuations of order 10%. Scans and polarizations were subsequently averaged, and a fifth-order polynomial baseline was fit to the full 50 MHz bandwidth and subtracted. Systematic flux calibration errors in these data are of order 10%. All data

⁷ AIPS++ is freely available for use under the Gnu Public License. Further information may be obtained from <http://aips2.nrao.edu>.

⁸ The National Radio Astronomy Observatory is a facility of the National Science Foundation operated under cooperative agreement by Associated Universities, Inc.

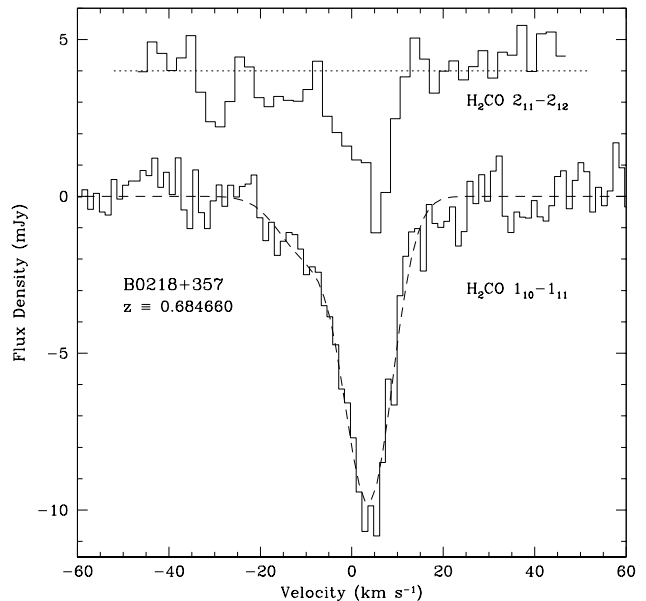


Figure 2. Formaldehyde 1₁₀-1₁₁ (6 cm) and 2₁₁-2₁₂ (2 cm) absorption toward the gravitational lens system B0218+357. The rest-frame velocity scale assumes a heliocentric redshift of $z = 0.684660$, and the spectral resolutions are 1.3 and 2.1 km s⁻¹ in the lower and upper lines, respectively. The dashed line shows a two-component Gaussian fit to the 6 cm line profile. The 2 cm line spectrum, also detected by Menten & Reid (1996), is offset by 4 mJy, with the zero point indicated by the dotted line.

reduction was performed in GBTIDL.⁹

3. RESULTS

The Arecibo spectrum of the 1₀₁-1₁₁ transition requires two Gaussian components for a good fit to the line profile (Figure 2). The rest frame velocity resolution is 1.3 km s⁻¹. Table 2 lists the two fit components and the properties of the total line. The total line properties are not based on Gaussian fits; they are computed directly from the spectrum. All velocities are in the rest frame with respect to a heliocentric redshift

⁹ GBTIDL (<http://gbtidl.nrao.edu/>) is the data reduction package produced by NRAO and written in the IDL language for the reduction of GBT data.

of $z = 0.68466$. The integrated optical depth in this transition is $0.239(8) \text{ km s}^{-1}$ over $-20 \text{ km s}^{-1} \leq \nu \leq +17 \text{ km s}^{-1}$ assuming a continuum of $650 \pm 16 \text{ mJy}$ and a unity covering factor (see Sections 4.1 and 4.2).

The GBT detection of the $2_{11}-2_{12}$ transition has a lower signal to noise ratio than the Arecibo $1_{10}-1_{11}$ transition. Despite this and the lower spectral resolution of the GBT spectrum (2.1 versus 1.3 km s^{-1}), both lines display similar profiles (Figure 2), although the $2_{11}-2_{12}$ detection is insufficient to justify a second profile component as seen in the $1_{10}-1_{11}$ spectrum and in the data of Jethava et al. (2007). The properties listed in Table 2 for this line have been measured directly from the data. The integrated optical depth, spanning the same velocity range as the 4.8 GHz line, is $0.083(10) \text{ km s}^{-1}$, assuming a continuum of $663 \pm 22 \text{ mJy}$ and a unity covering factor (see Sections 4.1 §4.2).

The observed profiles are narrower than the 15 km s^{-1} observed in CO, HCO^+ , and HCN (Combes & Wiklind 1996), but broader than the NH_3 lines that range from $6.6(1.6)$ to $9.3(1.8) \text{ km s}^{-1}$ (Henkel et al. 2005). OH spectra (1.67 GHz rest) clearly show a two-component profile (Kanekar et al. 2003), although at 20 and 27 km s^{-1} the line components are broader than the $\sim 10 \text{ km s}^{-1}$ H_2CO lines. Our detection of the $2_{11}-2_{12}$ transition is comparable to that of Menten & Reid (1996). Jethava et al. (2007) report a much narrower $1_{10}-1_{11}$ line — with a FWHM of $5.5(5) \text{ km s}^{-1}$ — but our high signal to noise ratio and resolution make our measurement more statistically robust. Both of our observations are coincident in velocity space with previous molecular detections in B0218+357.

4. ANALYSIS

4.1. Source Continuum

In general, while the continuum determinations may be uncertain and lead to errors in the absolute optical depth and total column density, the computation of quantities that depend on ratios of (low) optical depths, such as excitation temperatures and $n(\text{H}_2)$, will be significantly less affected, provided that systematic errors are consistent across frequency.

The continuum emission at 2.9 GHz (the frequency of the redshifted 4.8 GHz $1_{10}-1_{11}$ transition) is nearly flat as a function of frequency for images A and B (O’Dea et al. 1992; Patnaik et al. 1993) but steeper for the Einstein ring and the extended emission halo. At 5 GHz, the ratio of the two compact flat spectrum components A:B is ~ 3.0 and the Einstein ring emission accounts for 10%–20% of the total emission (O’Dea et al. 1992; Patnaik et al. 1993). The two sources show time variability with a 10.5 day period, but the variability is constrained to be $< 8\%$ at low frequencies (Mittal et al. 2006). Extended emission is detected at 1.465 and 1.63 GHz at the $\sim 10\%$ level, and additional structure is seen at 5 GHz (O’Dea et al. 1992; Patnaik et al. 1993).

Comparison to other molecules confirms the association of H_2CO absorption with image A (Menten & Reid 1996; Muller et al. 2007). The appropriate continuum level to use in apparent optical depth calculations for the $1_{10}-1_{11}$ transition is thus the total continuum at 2.9 GHz (8.6 GHz for the $2_{11}-2_{12}$ line) less image B, the Einstein ring emission, and any extended source structure. Interpolating the flux densities for images A and B and the extended emission from interferometric observations allows measurement of the fraction of the continuum from image A, a fraction crucial to disentangling the absorption in front of image A from the unabsorbed

continuum of image B and other extended structure.

The flux density of image A at 2.9 GHz can be interpolated from a linear fit (in the log) to the flux density versus frequency of image A. We use the very long baseline interferometry (VLBI) observations of Mittal et al. (2006) because these straddle 2.9 GHz and because these observations, of all the available interferometric measurements, were taken closest in time to our spectra (2002 January versus 2004 August for the Arecibo $1_{10}-1_{11}$ observations and 2006 April for the GBT $2_{11}-2_{12}$ observations). The continuum, interpolated from a fit to the image A data points spanning 2.25–15.35 GHz (the 1.65 GHz datum is dropped due to a steep downturn below 2.25 GHz; see Mittal et al. 2006), is $650 \pm 16 \text{ mJy}$, which neglects systematic and calibration errors typically of order 10%. The image A continuum is nearly flat, and interpolation error is less of a concern than overall flux calibration. Mittal et al. (2006) degrade their resolution to $50 \times 50 \text{ mas}$, comparable in resolution to MERLIN observations by Patnaik et al. (1993) to account for the loss of flux in VLBI observations, yielding similar flux densities to within 10%. Note that extrapolations from lower resolution (and much older) observations predict higher flux densities at 2.9 GHz: O’Dea et al. (1992) predict $868 \pm 64 \text{ mJy}$, and Patnaik et al. (1993) predict $791 \pm 68 \text{ mJy}$. We adopt $S_A(2.867 \text{ GHz}) = 650 \pm 16 \text{ mJy}$, bearing in mind that this estimate could potentially have large systematic errors. For the 14 GHz line redshifted to 8.6 GHz, we use the same VLBI data and continuum estimation method, adopting $S_A(8.600 \text{ GHz}) = 663 \pm 22 \text{ mJy}$. The VLBI observations of Mittal et al. (2006) are degraded to 10 mas at 8.4 GHz and 5 mas at 15 GHz.

4.2. Source Covering Factor

Calculation of the true optical depth of each line requires knowledge of the covering factor f_ν describing the fraction of image A obscured by the absorbing cloud at the line frequency ν . The covering factor corrects the observed line intensity to account for dilution of the line due to incomplete coverage of the continuum source by the absorbing cloud. Thus, the optical depth τ_{line} of the line takes the form

$$\tau_{\text{line}} = -\ln \left(1 - \frac{S_{\text{line}}}{f_\nu S_\nu} \right), \quad (1)$$

where S_{line} and S_ν are the line and continuum fluxes, respectively. Millimeter observations at $\nu > 100 \text{ GHz}$ show $f_\nu \gtrsim 0.77$ (Wiklind & Combes 1995), consistent with a covering factor of unity in front of image A and 0 in front of image B; the flux ratio (A/B) is close to 4 at 100 GHz (Muller et al. 2007).

Due to the increased solid angle of image A at lower frequencies (Mittal et al. 2006), the covering factors for the $1_{10}-1_{11}$ and $2_{11}-2_{12}$ transitions could be significantly less than unity even after excluding flux from image B and extended emission. Kanekar et al. (2003) estimate the covering factor to be 0.4 at 990 MHz (redshifted 18 cm OH), and Jethava et al. (2007) estimate the covering factor to be of the form $f_\nu = (\nu/100)^x$ for ν in GHz, determining that $0.0 < x < 0.5$ by interpolating between the millimeter observations of Wiklind & Combes (1995) and the 990 MHz OH observations of Kanekar et al. (2003). (Note that, in arriving at this range, they refer to the OH lines as being at 850 MHz, the redshifted frequency of the H I line.) For discussion, Jethava et al. (2007) adopt the most extreme frequency depen-

dence of $x = 0.5$, which gives covering factors of 0.17 and 0.29 for the $1_{10-1_{11}}$ and $2_{11-2_{12}}$ lines; the results they report are determined significantly by this choice of covering factors. Since this paper is concerned with excitation temperatures, which are determined via the ratio of the two lines, properly accounting for the frequency dependence of the covering factor is vital to obtaining accurate results.

VLBI observations of Mittal et al. (2006) show an extended source at low frequencies that splits image A into two point-like images separated at 15.4 GHz by ~ 1.4 mas, corresponding to a physical separation in the lensing galaxy of 9.6 pc (for a flat universe with $H_0 = 73 \text{ km s}^{-1} \text{ Mpc}^{-1}$, $\Omega_m = 0.27$, and $\Omega_\nu = 0.73$). The solid angle Ω_A follows a power law of index of $\alpha \approx -2.7$ (where $\Omega_A \propto \nu^\alpha$) as frequency increases from 1.65 to 15.65 GHz. (By comparing centimeter and millimeter observations, Henkel et al. (2005) argue that $-2 < \alpha < -1$.) The relatively flat spectrum of the south-western source in image A suggests that it is the flat-spectrum core of the quasar and the location of continuum emission seen in millimeter observations, where the frequency-dependent jet would not be observable (Patnaik et al. 1995). Since the core is fully obscured ($f_\nu = 1$) in millimeter observations, where the jet is not visible, the absorbing cloud lies along — but is not necessarily centered upon — the line of sight to it.

At 8.6 GHz, where the jet and the core are not distinctly separated, the $\sim 15 \text{ mas}^2$ region containing the core emits $\sim 60\%$ of the flux of image A (Patnaik et al. (1995) measure 62(1)% with VLBI observations at 15 GHz). The total area of image A with flux density 5 times the rms background, found by extrapolating from the VLBI observations of Mittal et al. (2006), is $\sim 32 \text{ mas}^2$ at this frequency. A spherical molecular cloud of 30 pc diameter subtends $\sim 15 \text{ mas}^2$ ($\sim 47\%$ of Ω_A at 8.6 GHz) at $z = 0.68$. Such a cloud gives a minimum covering factor of 0.3 if the core, which has $f_\nu = 1$ at millimeter frequencies, is obscured only by a limb of the cloud; due to the comparable line widths observed at both centimeter and millimeter frequencies (Jethava et al. 2007), it is likely that the absorbing cloud is fortuitously aligned with image A and that the covering factor is close to 0.6 for a 30 pc cloud. This is a strictly geometric argument, and weighting the covering factor by the fraction of flux that is obscured will give $f_{14.5} \geq 0.6$ even for somewhat smaller clouds.

The diameter of the cloud is likely to be significantly larger than 30 pc, since the optical obscuration of image A suggests the presence of large amounts of dust and possibly a giant molecular cloud (Grundahl & Hjorth 1995); Wiklind & Combes (1999) report a visual extinction of $A_v = 850$ in front of image A. Applying the relation between cloud size S (equivalent to diameter for a spherical cloud) in pc and velocity dispersion σ_v in km s^{-1} measured empirically with CO for Galactic clouds (Solomon et al. 1987) of

$$\frac{\sigma_v}{\text{km s}^{-1}} = 1.0 \pm 0.1 \left(\frac{D}{\text{pc}} \right)^{0.50 \pm 0.05}, \quad (2)$$

gives $S \approx 225 \text{ pc}$ (CO line widths are 15 km s^{-1} ; Wiklind & Combes 1995), suggesting a cloud much larger than the 650 mas^2 solid angle subtended by image A at 2.9 GHz. While Solomon et al. (1987) measure the relation for clouds with $S < 50 \text{ pc}$ and line widths $\lesssim 8 \text{ km s}^{-1}$, this is a strong indication that the cloud is quite large, increasing the probability of a high covering factor. Muller et al. (2007), with high spectral resolution HCO⁺ (2–1) observations, re-

solve the line into four $\sim 4.5 \text{ km s}^{-1}$ components, suggesting a clumpy medium of moderately sized clouds arrayed in front of image A, allowing the covering factor to remain constant or even increase with decreasing observation frequency (and increasing Ω_A). While the HCO⁺ observations reveal that it is not a single large absorbing cloud, the presence of multiple clouds still allows for high covering factors.

Agreement (1σ) between the observed optical depths and our LVG model (see Section 4.3) requires $f_{4.8} > 0.2$ for $f_{14.5} = 0.6$ and $f_{4.8} > 0.3$ for $f_{14.5} = 1.0$. Matching optical depths requires $0.5 < f_{4.8} < 1.0$ for $f_{14.5} = 0.6$ and $f_{4.8} = 0.5$ for $f_{14.5} = 1.0$. Although likely, $f_{4.8} < f_{14.5}$ cannot be set *a priori* due to the clumpy absorbing medium. In subsequent analysis, we discuss results spanning the range of viable covering factors.

4.3. Radiative Transfer Modeling

Formaldehyde is susceptible to non-LTE excitation in either direction (maser inversion or anti-inversion), so it is generally inappropriate to assume a single line excitation temperature for the molecule. It is generally also not valid to attribute a single excitation temperature to all of the centimeter $\Delta J = 0$ lines, since all line excitation temperatures can differ. We employ the still valid assumption of statistical equilibrium in these H₂CO lines but allow all line excitation temperatures to float.

We used an LVG radiative transfer model to find relative level populations up to the 40th rotational energy state (10_{37}) of o-H₂CO and the 41st (7_{43}) of p-H₂CO. Assuming statistical equilibrium, the model computes optical depths and excitation temperatures for a given formaldehyde density $n(\text{H}_2\text{CO})$ and a hydrogen density $n(\text{H}_2)$. The model assumes an isothermal and constant density spherically symmetric cloud with large-scale turbulence or gravitational collapse producing large velocity gradients. Following the observed velocity gradient of Solomon et al. (1987), we set the velocity gradient to $1.0 \text{ km s}^{-1} \text{ pc}^{-1}$. $N(\text{o-H}_2\text{CO})$ values scale inversely with the gradient dv/dr (Wang et al. 2004):

$$N(\text{o-H}_2\text{CO}) = [n(\text{o-H}_2\text{CO})/(dv/dr)] \times 3.08 \times 10^{18} \times \Delta\nu \\ = [n(\text{H}_2) \cdot X/(dv/dr)] \times 3.08 \times 10^{18} \times \Delta\nu, \quad (3)$$

where $\Delta\nu$ is the line width (FWHM), $n(\text{o-H}_2\text{CO})$ is the number density, and X is the abundance of o-H₂CO (not total H₂CO) relative to H₂. Since they are found via ratios of optical depths, which are proportional to $N(\text{o-H}_2\text{CO})$, $n(\text{H}_2)$ and T_{ex} results are independent of dv/dr . For a more thorough discussion of the LVG method, see Sobolev (1960) and Goldreich & Kwan (1974).

Our model includes non-LTE collisional excitation of H₂CO by H₂. We use the He collisional cross sections calculated by Green (1991) as a proxy for the aspherical H₂; Green notes that the substitution of He for H₂ could cause errors up to 50% in individual collisional excitation rates between levels, but that this is likely to translate to overall errors in level populations of order 20%. Using pressure-broadened H₂–H₂CO and He–H₂CO laboratory measurements of the millimeter transitions, Mengel & De Lucia (2000) find the He–H₂CO collision rates to be “very good,” while the collisional cross sections of H₂–H₂CO collisions are erroneous by up to a factor of 2 from the scaled collision rates ($\sqrt{\mu_{\text{H}_2}/\mu_{\text{He}}}$) with no apparent pattern to the errors.

We evaluated the effect on excitation temperatures of such an error in collision rates by randomly altering collision rates with Gaussian variation with a mean of zero and a standard

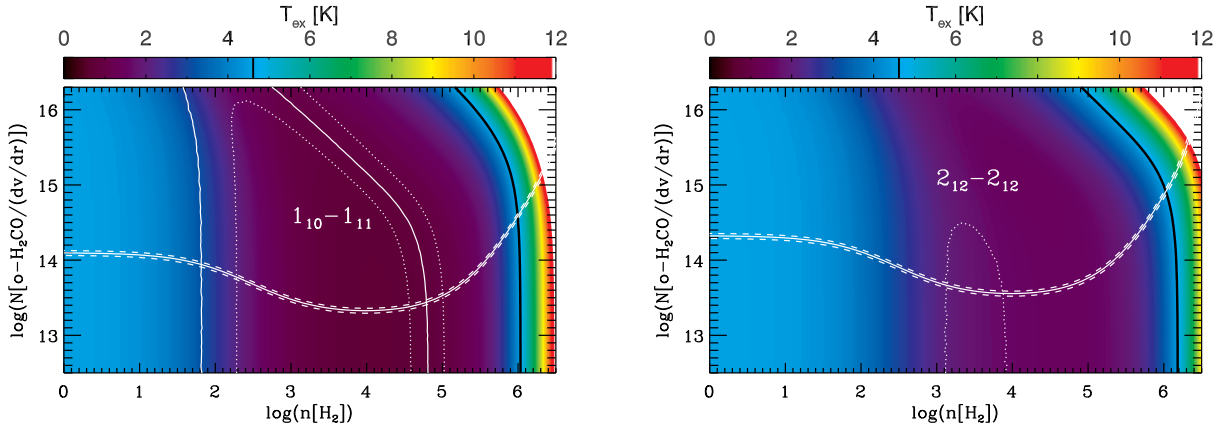


Figure 3. Contours trace excitation temperatures of the $1_{10}-1_{11}$ (left) and $2_{11}-2_{12}$ (right) transitions as a function of $n(\text{H}_2)$ and $N(\text{o-H}_2\text{CO})/(\text{km s}^{-1} \text{pc}^{-1})^{-1}$ as calculated with our LVG model. Overplotted white lines represent the observed peak optical depth of the $1_{10}-1_{11}$ line (\sim horizontal) and the ratio of observed peak optical depths of the $1_{10}-1_{11}$ and $2_{11}-2_{12}$ lines (\sim vertical) with 68% (1σ) confidence intervals. $T_{\text{CMB}} = 4.6$ K at $z = 0.68$, which we set as the background radiation temperature, and $T_{\text{kin}} = 55$ K (Henkel et al. 2005). The black line is the 4.6 K contour. CS observations and modeling firmly limit $n(\text{H}_2) < 2 \times 10^4 \text{ cm}^{-3}$ (Henkel et al. 2005) — the range of these plots exceed that limit to show the behavior of H_2CO as a function of $n(\text{H}_2)$ — and $T_{\text{ex}} < T_{\text{CMB}}$ for all points on the map below that limit. Column density (y-axis) is in units of $\text{cm}^{-2} (\text{km s}^{-1} \text{pc}^{-1})^{-1}$, and number density (x-axis) is in units of cm^{-3} . It is assumed throughout this paper that the velocity gradient dv/dr is $1 \text{ km s}^{-1} \text{pc}^{-1}$. The white at high $n(\text{H}_2)$ represents a ceiling to the contours at 12 K and not a physical plateau. The upper right corner of the $1_{10}-1_{11}$ plot reaches ~ 55 K, the kinetic temperature of the gas. Overplotted white lines on the $1_{10}-1_{11}$ plot represent the solution if covering factors are $f_{4.8} = 0.5$ and $f_{14.5} = 0.8$; the central region is excluded, while a cloud with negligible collisions — $\log(n[\text{H}_2]) = 0 \text{ cm}^{-3}$ — but unrealistic X is not excluded by the ratio of optical depths at the 68% confidence level if priors on X are neglected. The similar lines on the $2_{11}-2_{12}$ plot represent the constraints placed by observations if covering factors are $f_{4.8} = 0.3$ and $f_{14.5} = 1.0$; the central region is within the 68% confidence region although there is no solution in the model that exactly matches the observed lines. Differences in solutions shown on the two plots are due entirely to the selection of covering factors.

deviation of 50%. This overestimates the “up to 50%” error quoted by Green (1991) but is close to that measured by Mengel & De Lucia (2000). For each of 25 sets of “erroneous” collisional rates, we generated the parameter space shown in Figure 3. The effect of the errors on line excitation temperatures is small at low densities, where collisions are infrequent (Section 4.4); at moderate densities, the rms of the excitation temperatures of data sets is comparable to the mean excitation temperatures. For the density measurements reported herein (see below), the mean excitation temperatures of our erroneous data sets are 0.85 K for the $1_{10}-1_{11}$ transition and 1.4–1.7 K for the $2_{11}-2_{12}$ transition; rms values are 1.0 and 1.0–1.5, respectively. Taking an extreme scenario and uniformly doubling the collisional excitation rates of Green (1991) increases the effect of collisions at a given density, approximately halving the $n(\text{H}_2)$ values (0.3 dex) on the x-axis in Figure 3.

The model used to determine excitation temperatures was generated with an ambient radiation temperature of $T_{\text{CMB}} = 2.73(1+z) = 4.60$ K and a kinetic temperature of 55 K. With a parameter space spanning $1 \text{ cm}^{-3} < n(\text{H}_2) < 10^7 \text{ cm}^{-3}$ and $3 \times 10^{12} \text{ cm}^{-2} (\text{km s}^{-1} \text{pc}^{-1})^{-1} < N(\text{o-H}_2\text{CO})/(dv/dr) < 3 \times 10^{16} \text{ cm}^{-2} (\text{km s}^{-1} \text{pc}^{-1})^{-1}$ with a sampling interval of 0.05 dex, we compared the observed peak optical depths to those generated with our LVG model. The model is weakly dependent on kinetic temperature: changes in modeled optical depth are less than observational error for $T_K = 55 \pm 20$ K, and we present results only for $T_{\text{kin}} = 55$ K, as measured via NH_3 observations by Henkel et al. (2005).

Of the four spectral components Muller et al. (2007) identify in their high resolution HCO^+ spectrum, the strongest absorption occurs at the same velocity as both the $\text{H}_2\text{CO } 2_{11}-2_{12}$ line and the strongest component of the $1_{10}-1_{11}$ profile. The ratio of the strongest $1_{10}-1_{11}$ absorption component and the $2_{11}-2_{12}$ line allows *in situ* densitometric measurements: the optical depth of one transition gives $N(\text{o-H}_2\text{CO})$, and the ratio of two K -doublets gives $n(\text{H}_2)$. Thus, with the two lines

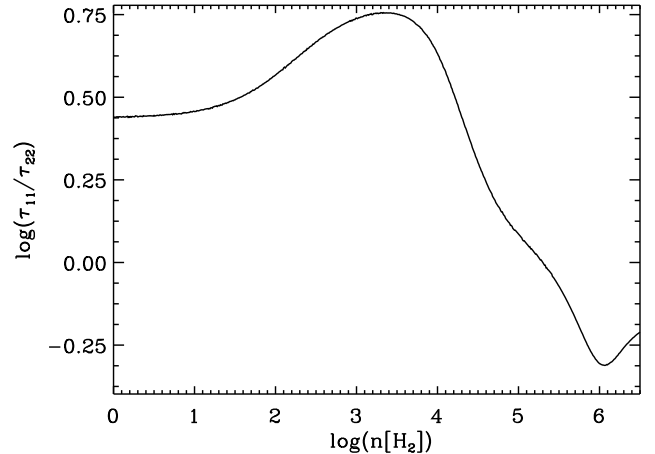


Figure 4. Ratio of the optical depth of the $1_{10}-1_{11}$ transition to that of the $2_{11}-2_{12}$ transition as a function of $n(\text{H}_2)$. The modeled optical depths assume covering factors of unity and a constant H_2CO abundance relative to H_2 of $X = 10^{-9}$. The two-line densitometry method cannot produce unique results in regions where a single value of the optical depth ratio corresponds to two values of $n(\text{H}_2)$ unless the density is constrained by priors or ancillary information. The non-unique region is enlarged if X is not assumed to be constant, as can be seen in the two viable density regions plotted in the left image of Figure 3, where the two possible densities are $n(\text{H}_2) \approx 6 \times 10^4 \text{ cm}^{-3}$ (with $X \approx 10^{-11}$) and $n(\text{H}_2) \approx 60 \text{ cm}^{-3}$ (with $X \approx 3 \times 10^{-8}$). If priors can discriminate between $n(\text{H}_2) \lesssim 2.5 \times 10^3 \text{ cm}^{-3}$ and $n(\text{H}_2) \gtrsim 2.5 \times 10^3 \text{ cm}^{-3}$, solutions are unique and H_2CO is a powerful densitometer.

one can define a region of the modeled parameter space by matching observed optical depths to modeled ones. When $n(\text{H}_2) \lesssim 2 \times 10^4$, the ratio of lines can result in bifurcated solutions for $n(\text{H}_2)$ when using the two-line densitometry method employed herein — one at moderate $n(\text{H}_2)$ and one at low $n(\text{H}_2)$, as is shown in Figure 4.

To break the degeneracy of solutions using observations of other molecules and abundance arguments, we divide the

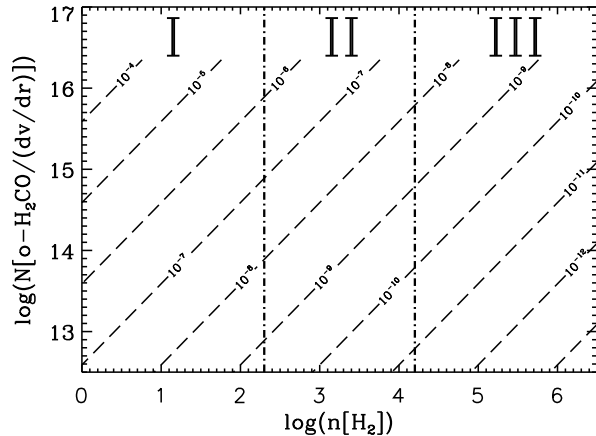


Figure 5. Diagonal dashed lines mark the abundance of o-H₂CO relative to H₂ (see Equation 3); vertical dot-dashed lines separate the regions, labeled at top, discussed in Section 4.3 and Table 3. Typical Galactic abundances are of order 10^{-9} , while measurements of $N(\text{H}_2\text{CO})$ (Jethava et al. 2007) and $N(\text{H}_2)$ (Combes & Wiklind 1995; Gerin et al. 1997) place the total H₂CO abundance between 2.5×10^{-9} and 10^{-10} in B0218+357; the ortho/para ratio, which Jethava et al. (2007) measure as ~ 2.8 , drops the abundance of o-H₂CO by $\sim 25\%$ relative to the total abundance of H₂CO.

possible solutions into three regions separated at $n(\text{H}_2) = 2 \times 10^2 \text{ cm}^{-3}$ and $n(\text{H}_2) = 2 \times 10^4 \text{ cm}^{-3}$, as shown in Figure 5 and described in Table 3. The Region I/II boundary at $n(\text{H}_2) = 2 \times 10^2$ is an arbitrary division between low densities, where $T_{\text{ex}} \approx T_{\text{CMB}}$ for both the $1_{10}-1_{11}$ and $2_{11}-2_{12}$ transitions, and moderate densities, where $T_{\text{ex}} < T_{\text{CMB}}$. The Region II/III boundary at $n(\text{H}_2) = 2 \times 10^4 \text{ cm}^{-3}$ is the firm upper limit placed by CS observations and modeling (Henkel et al. 2005). Ranges of abundances in each region are calculated for all covering factors for which equilibrium model solutions exist, determining $N(\text{o-H}_2\text{CO})$ and $n(\text{H}_2)$ for all covering factors within these ranges, and converting column densities to number densities of o-H₂CO with Equation 3; maximum and minimum abundance values (X , Equation 3) listed in Table 3 are the maximum and minimum values of $n(\text{o-H}_2\text{CO})/n(\text{H}_2)$ in each region. Due to the high abundance ($\log[X] > -8.2$), the low-density Region I is unlikely: typical Galactic abundances have a small dispersion around a few $\times 10^{-9}$ (e.g., Evans et al. 1975; Dickel, Goss, & Rots 1987). Measurements of $N(\text{H}_2\text{CO})$ (Jethava et al. 2007) and $N(\text{H}_2)$ (Combes & Wiklind 1995; Gerin et al. 1997) in B0218+357 place the total H₂CO abundance between 2.5×10^{-9} and 10^{-10} in B0218+357; the ortho/para ratio, which Jethava et al. (2007) measure as 2.8 in their best model of the lines they observed, drops the abundance of o-H₂CO by $\sim 25\%$ from the total H₂CO abundance. These constraints agree with the value of $n(\text{H}_2) \approx 3.2 \times 10^3 \text{ cm}^{-3}$ estimated from NH₃ (Henkel et al. 2005, no confidence interval given).

Fitting observed optical depths to our LVG model within the above constraints and forcing $f_{14.5} > 0.6$ gives $2 \times 10^3 \text{ cm}^{-3} < n(\text{H}_2) < 1 \times 10^4 \text{ cm}^{-3}$ (1σ) for the covering factors discussed above. Agreement between observations and modeling requires $f_{4.8}/f_{14.5} \gtrsim 1/3$, while the ratio of solid angles in image A is $\Omega_{4.8}/\Omega_{14.5} \approx 20$. Since the covering factors are poorly constrained, results for $n(\text{H}_2)$ and T_{ex} cannot have proper confidence intervals. However, our reported ranges include all reasonable covering factors ($f_{14.5} > 0.6$, $f_{4.8}/f_{14.5} \gtrsim 1/3$) and are thus robust. We list $n(\text{H}_2)$ and T_{ex}

Table 3
Formaldehyde Radiative Transfer Model Regions: H₂ Number Density and H₂CO Abundance

Region	Min. $\log(n(\text{H}_2))$	Max. $\log(n(\text{H}_2))$	Min. $\log(X)$	Max. $\log(X)$
I	0.0	2.3	-8.2	-5.6
II	2.3	4.3	-10.2	-8.2
III	4.3	5.5	-10.3	-10.2

Note. — Molecular hydrogen densities $n(\text{H}_2)$, with units of cm^{-3} , and o-H₂CO abundances X (Equation 3) at the boundaries between the regions discussed in Section 4.3 and shown in Figure 5. The Region I/II boundary is an arbitrary division between low densities, where $T_{\text{ex}} \approx T_{\text{CMB}}$, and moderate densities, where $T_{\text{ex}} \ll T_{\text{CMB}}$. The Region II/III boundary is the upper limit placed by CS observations and modeling Henkel et al. (2005). Ranges of abundances are calculated by determining $N(\text{o-H}_2\text{CO})$ and $n(\text{H}_2)$ for all covering factors with equilibrium model solutions within these ranges, and converting column densities to number densities of o-H₂CO with Equation 3; maximum and minimum X values are the maximum and minimum values of $n(\text{H}_2\text{CO})/n(\text{H}_2)$ in each region. The typical H₂CO abundance relative to H₂ in Galactic molecular clouds is $\sim 10^{-9}$, and the ortho/para ratio ranges from 1 to 3. In B0218+357, the total H₂CO abundance is $1-25 \times 10^{-10}$, assuming an ortho/para ratio of 2.8.

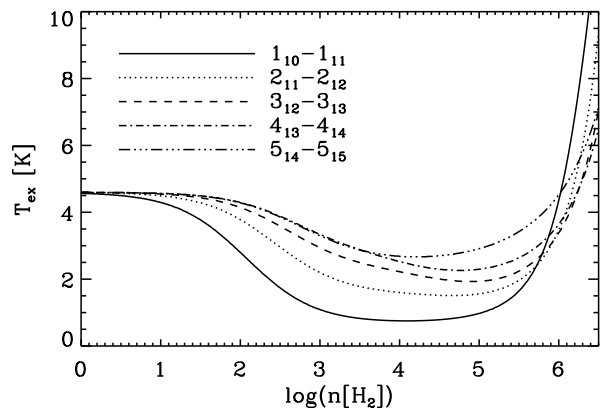


Figure 6. Excitation temperatures of the lowest five K -doublet transitions as a function of $n(\text{H}_2)$ for $N(\text{o-H}_2\text{CO}) = 10^{14} \text{ cm}^{-2}$, as calculated with our LVG model. This figure is a horizontal slice through Figure 3 with additional K -doublet lines added. The divergence of the K -doublet excitation temperatures as a function of $n(\text{H}_2)$ makes the ratio of any pair of lines a sensitive densitometer. However, since the ratios converge to unity at low $n(\text{H}_2)$ (as T_{ex} approaches T_{CMB}) and cross it again at $n(\text{H}_2) \approx 10^6$ (as all excitation temperatures go to T_{kin} at high densities), the ratios cannot provide a unique global solution unless the covering factor is known *a priori* or other information, such as observations of other molecules, is available to break the degeneracy (Section 4.3).

for various covering factors in Tables 4–6; $T_{\text{ex}} < T_{\text{CMB}}$ for all physical pairs of covering factors.

4.4. Column Density and Excitation Temperatures

We find $2.5 \times 10^{13} \text{ cm}^{-2} < N(\text{o-H}_2\text{CO}) < 8.9 \times 10^{13} \text{ cm}^{-2}$ (assuming a velocity gradient of $1 \text{ km s}^{-1} \text{ pc}^{-1}$), with the range determined by the viable covering factors ($f_{14.5} > 0.6$, $f_{4.8}/f_{14.5} \gtrsim 1/3$) and constraints on molecular hydrogen densities ($2 \times 10^3 \text{ cm}^{-3} < n(\text{H}_2) < 1 \times 10^4 \text{ cm}^{-3}$). Since these results cover all reasonable covering factors, the limits are hard and conservative. The total H₂CO column density, assuming o-H₂CO/p-H₂CO = 2.8 from the best models of Jethava et al. (2007), which is determined primarily from millimeter observations where covering factors are unity and not a concern, is $3.4 \times 10^{13} - 1.2 \times 10^{14} \text{ cm}^{-2}$. The column density scales inversely with the assumed velocity gradient.

Table 4
Model-Derived Number and Column Densities For
Various Covering Factors

$f_{4.8}$	$f_{14.5}$	$\log(n(\text{H}_2))$ (cm^{-3})	$\log(N(o\text{-H}_2\text{CO})/(dv/dr))$ ($\text{cm}^{-2} (\text{km s}^{-1} \text{pc}^{-1})^{-1}$)
0.50	0.60	$5.05^{+0.15}_{-0.15}$	$13.55^{+0.10}_{-0.10}$
		$0.03^{+1.47}_{-0.03}$	$14.10^{+0.00}_{-0.10}$
0.50	0.80	$4.80^{+0.20}_{-0.20}$	$13.45^{+0.10}_{-0.05}$
		$1.80^{+0.45}_{-1.80}$	$13.95^{+0.15}_{-0.15}$
0.30	1.00	$3.53^{+0.37}_{-0.38}$	$13.60^{+0.05}_{-0.05}$
1.00	1.00	$5.15^{+0.15}_{-0.10}$	$13.30^{+0.10}_{-0.05}$

Note. — Confidence intervals are set at 1σ (68%) but are non-Gaussian. Where more than one solution exists within 1σ observational error, all solutions are given. An error of ‘0.00’ indicates that the modeled density did not change significantly across the region of density space defined by fitting observed optical depths to those derived with our LVG model. Number densities above $2 \times 10^4 \text{ cm}^{-3}$ contradict the firm upper limit obtained from LVG models of CS observations (Henkel et al. 2005).

Regardless of covering factors (although tables herein only list several, the entire range of reasonable covering factors was evaluated), Figure 3 shows that the excitation temperatures of both observed lines are below T_{CMB} within the constraints placed by CS, which require $n(\text{H}_2) \lesssim 2 \times 10^4 \text{ cm}^{-3}$. Figures 3 and 6 show clearly that, at $z = 0.68$, the H_2CO centimeter lines will be anti-inverted. The non-LTE excitation is density dependent:

1. $n(\text{H}_2) \lesssim 10^2 \text{ cm}^{-3}$: H_2CO excitation is dominated by CMB photons. All excitation temperatures are held near to the microwave background and the system is nearly in radiative equilibrium with the CMB because collisions with H_2 are too infrequent to pump the H_2CO K -doublet population into anti-inversion.
2. $10^2 \text{ cm}^{-3} \lesssim n(\text{H}_2) \lesssim 3 \times 10^5 \text{ cm}^{-3}$: Collisions with H_2 anti-invert the H_2CO K -doublet population. The millimeter transitions, however, have $T_{\text{ex}} \geq T_{\text{CMB}}$.
3. $n(\text{H}_2) \gtrsim 3 \times 10^5 \text{ cm}^{-3}$: High densities increase collision rates and drive H_2CO toward thermal equilibrium with H_2 , with a kinetic temperature of 55 K.

Figure 6, a horizontal slice through Figure 3, shows a ‘U’ shape of excitation temperatures. The two possible values of T_{ex} and $n(\text{H}_2)$ for a given ratio of observed optical depths cause the degeneracy discussed in Section 4.3 and shown in Figure 4. The $n(\text{H}_2)$ -dependence of centimeter excitation temperatures makes H_2CO a sensitive *in situ* densitometer if the degeneracy can be broken with *a priori* knowledge of physical conditions such as H_2CO abundance or limits on $n(\text{H}_2)$.

5. DISCUSSION

5.1. Comparison to Excitation in Galactic Molecular Clouds

Galactic dark clouds show a decrement in the excitation temperature of the $1_{10}\text{--}1_{11}$ line relative to the CMB of $T_{\text{ex}} - T_{\text{CMB}} \simeq -0.7$ to -0.4 K (Evans et al. 1975). An LVG radiative transport model applied to Galactic giant molecular clouds derives comparable decrements, ranging from -1 to 0 K (Henkel et al. 1980). The cloud studied in this paper shows a much larger decrement, with $T_{\text{ex}} - T_{\text{CMB}} \lesssim -3.6$ K (for

$2 \times 10^3 \text{ cm}^{-3} < n(\text{H}_2) < 1 \times 10^4 \text{ cm}^{-3}$). For the $2_{11}\text{--}2_{12}$ transition, the decrement is ~ -2.6 to -3.1 K. The magnified decrement is due to the collisional dependence of excitation temperatures (Section 4.4): CMB excitation is only significant in diffuse clouds with $n(\text{H}_2) \lesssim 10^2 \text{ cm}^{-3}$, so for higher density clouds the excitation temperature is nearly constant regardless of the CMB temperature. Increasing the background temperature thus magnifies the $T_{\text{ex}} - T_{\text{CMB}}$ decrement proportionally to $(1+z)$.

Because $T_{\text{ex}} - T_{\text{CMB}} < 0$ for both transitions, the cloud would be observable in absorption against the CMB in both lines without the background quasar – if the cloud were in a different place in the lensing galaxy rather than aligned with image A or in a galaxy with no background continuum source, for instance. In the case where the cloud is matched to the telescope beam (no beam dilution) at $z = 0.68$ and the covering factor is unity, the observed $1_{10}\text{--}1_{11}$ line temperature would be

$$T_{\text{line}} = (1 - e^{-\tau})(T_{\text{ex}} - T_{\text{CMB}})/(1+z) \approx -36 \text{ mK}. \quad (4)$$

For a non-unity covering factor and small optical depth, as seen in B0218+357, T_{line} is approximately inversely proportional to the covering factor. Such a cloud illuminated by the CMB will be observable with future instruments such as the EVLA. Since T_{ex} is small and nearly constant with redshift and T_{CMB} scales as $1+z$, this raises the possibility of surveying molecular gas in galaxies *regardless of distance* or chance alignment with sources of background illumination.

Models indicate that the anti-inversion persists in the $K_a = 1$ K -doublets at least up to the $6_{15}\text{--}6_{16}$ $o\text{-H}_2\text{CO}$ transition for all reasonable covering factors (which determine the measured molecular hydrogen density), and for some covering factors the anti-inversion persists into the $7_{16}\text{--}7_{17}$ transition (Table 5). Although the highest energy lines may be difficult to detect, all of the anti-inverted transitions should in principle be observable in absorption against the CMB.

K -doublet transitions with $K_a = 2$ ($p\text{-H}_2\text{CO}$) and $K_a = 3$ ($o\text{-H}_2\text{CO}$) are even more strongly anti-inverted than those in the $K_a = 1$ ladder, but relative to the $K_a = 1$ K -doublets the higher energy of the $K_a > 1$ states (the lowest $K_a = 2$ K -doublet level, 2_{21} at 57.6 K, has approximately the same energy as the 5_{15} level at 62.5 K) generally makes them more optically thin and difficult to observe given the low temperatures of molecular clouds. Our models indicate that the $2_{20}\text{--}2_{21}$ transition (71.1 MHz rest frequency), the lowest K -doublet of the $K_a = 2$ ladder, has an excitation temperature less than 10 mK in B0218+357. Due to the relatively warm temperature of the gas observed in B0218+357 (55 K), the optical depth of the transition is predicted to be lower than that of the observed $1_{10}\text{--}1_{11}$ $o\text{-H}_2\text{CO}$ line by only a factor of ~ 5 and higher by a factor of ~ 20 than would be expected in an otherwise equivalent cloud with a kinetic temperature of 15 K (assuming an ortho/para ratio of 2.8; Jethava et al. 2007). The next lowest K -doublet of the $K_a = 2$ ladder, the $3_{21}\text{--}3_{22}$ transition (355.6 MHz rest), is predicted to have an optical depth that is an order of magnitude lower than that of the $2_{20}\text{--}2_{21}$ line. All other $K_a > 1$ K -doublets are weaker by yet another order of magnitude or more than the $3_{21}\text{--}3_{22}$ line. In the hypothetical case of a similar gas-rich galaxy illuminated only by the CMB at $z = 0.68$ (the flux from the quasar illuminating B0218+357 is not well known at meter wavelengths), the observed line temperatures for the lowest $K_a = 2$ K -doublets are predicted to be between -4 and -11

Table 5
Modeled K -doublet ($\Delta J = 0$) o-H₂CO Line Excitation Temperatures

$f_{4.8}$	$f_{14.5}$	$\log(n(\text{H}_2))$ (cm ⁻³)	$1_{10-1_{11}}$ 4.8 GHz	$2_{11-2_{12}}$ 14.5 GHz	$3_{12-3_{13}}$ 29.0 GHz	$4_{13-4_{14}}$ 48.3 GHz	$5_{14-5_{15}}$ 72.4 GHz	$6_{15-6_{16}}$ 101.3 GHz	$7_{16-7_{17}}$ 135.0 GHz
0.50	0.60	$5.05^{+0.15}_{-0.15}$	$0.97^{+3.26}_{-0.09}$	$1.57^{+2.90}_{-0.03}$	$1.98^{+2.55}_{-0.01}$	$2.34^{+2.22}_{-0.04}$	$2.94^{+1.61}_{-0.11}$	$3.63^{+0.76}_{-0.14}$	$4.77^{+0.20}_{-0.79}$
		$0.03^{+1.47}_{-0.03}$	$4.57^{+0.00}_{-1.23}$	$4.59^{+0.00}_{-0.51}$	$4.59^{+0.00}_{-0.28}$	$4.60^{+0.00}_{-0.19}$	$4.60^{+0.00}_{-0.20}$	$4.58^{+0.00}_{-0.65}$	$4.41^{+0.00}_{-0.48}$
0.50	0.80	$4.80^{+0.20}_{-0.20}$	$0.84^{+3.42}_{-0.06}$	$1.53^{+2.95}_{-0.00}$	$1.98^{+2.57}_{-0.01}$	$2.29^{+2.27}_{-0.00}$	$2.79^{+1.77}_{-0.07}$	$3.43^{+1.00}_{-0.12}$	$4.53^{+0.20}_{-0.53}$
		$1.80^{+0.45}_{-1.80}$	$3.24^{+1.33}_{-0.99}$	$4.03^{+0.56}_{-0.63}$	$4.30^{+0.29}_{-0.43}$	$4.40^{+0.20}_{-0.30}$	$4.39^{+0.21}_{-0.31}$	$3.92^{+0.66}_{-0.44}$	$3.93^{+0.48}_{-0.03}$
0.30	1.00	$3.53^{+0.37}_{-0.38}$	$0.80^{+3.34}_{-0.05}$	$1.75^{+2.68}_{-0.10}$	$2.51^{+2.01}_{-0.20}$	$2.89^{+1.66}_{-0.27}$	$2.87^{+1.67}_{-0.16}$	$3.06^{+1.29}_{-0.00}$	$3.93^{+0.07}_{-0.04}$
1.00	1.00	$5.15^{+0.15}_{-0.10}$	$1.04^{+3.31}_{-0.08}$	$1.60^{+2.91}_{-0.03}$	$2.01^{+2.55}_{-0.03}$	$2.39^{+2.18}_{-0.05}$	$3.03^{+1.54}_{-0.10}$	$3.76^{+0.71}_{-0.14}$	$4.92^{+0.25}_{-0.90}$

Note. — Excitation temperatures for selected pairs of covering factors $f_{4.8}$ and $f_{14.5}$; boldfaced temperatures have $T_{\text{ex}} \geq T_{\text{CMB}}$ ($T_{\text{CMB}} = 4.60$ K) within the listed 68% (non-Gaussian) confidence intervals. Frequencies are rest frequencies, and all excitation temperatures have units of K. Regions listed with errors of ‘0.00’ do not change excitation temperature significantly across the region of density space defined by fitting observed optical depths to those derived with our LVG model. Multiple excitation temperatures for a given pair of covering factors correspond to solutions in Table 4 where a pair of optical depths did not produce a unique solution. Low density solutions ($n(\text{H}_2) < 10^2$ cm⁻³) have $T_{\text{ex}} = T_{\text{CMB}}$ ($\tau = 0.68466$) = 4.60 K because collisions are insufficient to be a significant excitation mechanism. Of the K -doublet transitions, only the $1_{10-1_{11}}$ and $2_{11-2_{12}}$ lines have been observed in B0218+357 (see Table 2).

Table 6
Modeled $\Delta J = 1$ H₂CO Line Excitation Temperatures

$f_{4.8}$	$f_{14.5}$	$\log(n(\text{H}_2))$ (cm ⁻³)	$2_{12-1_{11}}$ (O) 140.8 GHz	$2_{11-1_{10}}$ (O) 150.5 GHz	$1_{01-0_{00}}$ (P) 72.8 GHz	$2_{02-1_{01}}$ (P) 145.6 GHz
0.50	0.60	$5.05^{+0.15}_{-0.15}$	$7.73^{+1.45}_{-3.13}$	$6.70^{+0.89}_{-2.10}$	$17.40^{+14.90}_{-12.80}$	$6.74^{+0.84}_{-2.14}$
		$0.03^{+1.47}_{-0.03}$	$4.60^{+0.00}_{-0.00}$	$4.60^{+0.00}_{-0.00}$	$4.60^{+0.00}_{-0.00}$	$4.60^{+0.00}_{-0.00}$
0.50	0.80	$4.80^{+0.20}_{-0.20}$	$6.31^{+1.06}_{-1.71}$	$5.78^{+0.69}_{-1.18}$	$9.77^{+5.23}_{-5.17}$	$5.84^{+0.67}_{-1.24}$
		$1.80^{+0.45}_{-1.80}$	$4.60^{+0.00}_{-0.00}$	$4.60^{+0.00}_{-0.00}$	$4.60^{+0.01}_{-0.00}$	$4.60^{+0.00}_{-0.00}$
0.30	1.00	$3.53^{+0.37}_{-0.38}$	$4.73^{+0.06}_{-0.13}$	$4.68^{+0.05}_{-0.08}$	$4.88^{+0.16}_{-0.28}$	$4.70^{+0.05}_{-0.10}$
1.00	1.00	$5.15^{+0.15}_{-0.10}$	$8.63^{+1.97}_{-4.03}$	$7.26^{+1.14}_{-2.66}$	$25.20^{+42.70}_{-20.60}$	$7.27^{+1.08}_{-2.67}$

Note. — Similar to Table 5 but for $\Delta J = 1$ transitions of both o-H₂CO (O) and p-H₂CO (P). All excitation temperatures have units of K. All transitions in this table have been observed in B0218+357 (Jethava et al. 2007). Low density solutions ($n(\text{H}_2) < 10^2$ cm⁻³) have $T_{\text{ex}} = T_{\text{CMB}}$ ($\tau = 0.68466$) = 4.60 K because collisions are insufficient to be a significant excitation mechanism.

mK for the $2_{20-2_{21}}$ line and -0.3 and -1 mK for the $3_{21-3_{22}}$ line (assuming $N(\text{H}_2\text{CO}) = 5 \times 10^{13}$ cm⁻² and an ortho/para ratio of 2.8, with the range set by our measured range of values for the molecular hydrogen density in the cloud). While these low-frequency lines will be dwarfed by the foreground Galactic continuum and difficult to observe for their own sake, this modeling indicates that H₂CO $K_a = 2$ absorption lines in gas-rich galaxies present potential contaminants to Epoch of Reionization studies.

5.2. Comparison to Previous Results

Jethava et al. (2007) measure $N(\text{o-H}_2\text{CO}) = 3.8 \times 10^{13}$ cm⁻² and $n(\text{H}_2) < 10^3$ cm⁻³ (with a best fit of $n(\text{H}_2) = 200$ cm⁻³) with their non-LTE LVG analysis of six H₂CO lines in B0218+357. Menten & Reid (1996), assuming LTE, measure $N(\text{o-H}_2\text{CO}) = 1.2 \times 10^{13}$ cm⁻² from their observation of the $2_{11-2_{12}}$ line, although they estimate that anti-inversion of the K -doublet would reduce their result by 50%, well below the column densities reported by Jethava et al. (2007) and our range of $2.5 \times 10^{13} - 8.9 \times 10^{13}$ cm⁻² (for $dv/dr = 1$ km s⁻¹ pc⁻¹).

Our $1_{10-1_{11}}$ spectrum has a significantly higher signal to noise ratio and better spectral resolution than previous obser-

vations, and reliance solely on it and our new $2_{11-2_{12}}$ data to determine densities precludes high-frequency atmospheric variability while magnifying the effect of uncertain covering factors. Since the centimeter K -doublet lines measure $n(\text{H}_2)$ with greater precision than the millimeter lines can, the trade-off makes the Jethava et al. (2007) result less accurate for determining $n(\text{H}_2)$ and T_{ex} (which they do not address) but more reliable for measuring $N(\text{o-H}_2\text{CO})$, since they rely heavily on nearly thermal millimeter transitions which have covering factors of unity. The optimal combination of the two methods uses the centimeter lines to constrain $n(\text{H}_2)$ (and T_{ex} , since it is closely related) and the millimeter lines to constrain $N(\text{o-H}_2\text{CO})$. T_{ex} and $n(\text{H}_2)$ are nearly independent of $N(\text{o-H}_2\text{CO})$ at the column densities observed in this source (Figure 3).

Our grid-search method is a more comprehensive analysis of the $n(\text{H}_2)$ - $N(\text{o-H}_2\text{CO})$ density space than that used by Jethava et al. (2007), who compared their observations only to LVG models with $n(\text{H}_2) = 0, 200, 500, 1000,$ and 3000 cm⁻³ to determine a best-fit (χ^2) value. The small values of $n(\text{H}_2)$ sampled by Jethava et al. (2007) also neglect the high- $n(\text{H}_2)$ solutions discussed in Section 4.3, essentially assuming their conclusion that the absorbing cloud is diffuse and low-density

and not considering the alternative higher density regime.

6. CONCLUSIONS

With new measurements of the $1_{10}-1_{11}$ and $2_{11}-2_{12}$ transitions of H_2CO in B0218+357, we have measured the molecular hydrogen number density and H_2CO column density. Using an LVG model of the physical conditions of the absorbing cloud in the gravitational lens and assuming a velocity gradient of $1 \text{ km s}^{-1} \text{ pc}^{-1}$, we measure $N(\text{o-H}_2\text{CO})$ to be in the range $2.5 \times 10^{13} - 8.9 \times 10^{13} \text{ cm}^{-2}$, where the uncertainty in values is caused by the uncertainty in covering factors (in the optically thin limit, the column density is inversely proportional to the covering factor). Jethava et al. (2007) measure an ortho/para ratio of 2.0–3.0 (with a best value of 2.8) and a second component to the profile that adds $\sim 15\%$ to the total column density; these two contributions increase the total column $N(\text{H}_2\text{CO})$ by $\sim 55\%$ above our measurement of $N(\text{o-H}_2\text{CO})$ in the primary absorption component. Since collisions with hydrogen are the dominant excitation mechanism, we are also able to measure $n(\text{H}_2) = 2 \times 10^3 - 1 \times 10^4 \text{ cm}^{-3}$, which again spans the range of viable covering factors.

Modeled excitation temperatures show both observed centimeter lines to be anti-inverted relative to the 4.6 K CMB at $z = 0.68$, with $T_{\text{ex}}(1_{10}-1_{11}) \approx 1 \text{ K}$ and $T_{\text{ex}}(2_{11}-2_{12}) \lesssim 2 \text{ K}$. Excitation temperatures of the millimeter lines are $\geq 4.60 \text{ K}$, as expected. These results show that the dominant absorbing cloud in the B0218+357 lens is analogous to Galactic molecular clouds that show anti-inversion of the K -doublet transitions, and the centimeter H_2CO lines could be observed *in absorption against the CMB* if the background source was removed or if the cloud was viewed along a different line of sight.

Since T_{ex} is determined by collisions in dense clouds, the source-frame decrement $T_{\text{ex}} - T_{\text{CMB}}$ is magnified when T_{CMB} is increased (n.b., at high redshift). The anti-inverted centimeter transitions thus could provide absorption lines against the CMB that would trace molecular gas *independently of distance* when observed with a telescope capable of resolving the star-forming regions in galaxies. Future work targeting additional objects will quantify the change in $T_{\text{ex}} - T_{\text{CMB}}$ with redshift and test these results.

We are indebted to C. Henkel for providing the LVG code used in this analysis and to the anonymous referee who suggested that we model the excitation temperatures of $K_a > 1$ K -doublets and checked our calculations with an independent radiative transfer code.

Support for this work was provided by NASA through Hubble Fellowship grant no. HST-HF-01183.01-A awarded by the Space Telescope Science Institute, which is operated by the Association of Universities for Research in Astronomy, Incorporated, under NASA contract NAS5-26555. We also acknowledge the support of the NSF through award GSSP07-0015 from the NRAO and NSF grant AST-0707713.

The LUNAR consortium (<http://lunar.colorado.edu>), headquartered at the University of Colorado, is funded by the NASA Lunar Science Institute (via Cooperative Agreement NNA09DB30A)

to investigate concepts for astrophysical observatories on the Moon.

This research has made use of the NASA/IPAC Extragalactic Database (NED) which is operated by the Jet Propulsion Laboratory, California Institute of Technology, under contract with the National Aeronautics and Space Administration.

REFERENCES

- Araya, E. D., Hofner, P., Goss, W. M., Linz, H. & Kurtz, S. & Olmi, L. 2008, *ApJS*, 178, 330
- Browne, I. A., Patnaik, A. R., Walsh, D. & Wilkinson, P. N. 1993, *MNRAS*, 263, L32
- Carilli, C. L., Rupen, M. P., & Yanny, B. 1993, *ApJ*, 412, L59
- Cohen, J. G., Lawrence, C. R., & Blandford, R. D 2003, *ApJ*, 583, 67
- Combes, F. & Wiklind, T. 1995, *A&A*, 299, 382
- Combes, F. & Wiklind, T. 1996, in *Cold Gas at High Redshift*, ed. M. Bremer H. Rottgering, P. van der Werf, & C. L. Carilli (Dordrecht: Kluwer), 215
- Combes, F. & Wiklind, T. 1997, *ApJ*, 486, L79
- Dickel, H. R., Goss, W. M., & Rots, A. H. 1987, in *IAU Symp. No. 120, Astrochemistry*, ed. M. S. Vardya & S. P. Tarafoder (Dordrecht: Reidel), 185
- Dickens, J. E. & Irvine, W. M. 1999, *ApJ*, 518, 733.
- Evans, N. J. II, Zuckerman, B, Morris, G., & Sato, T. 1975, *ApJ*, 196, 433
- Garrison, B. J., Lester Jr., W. A., Miller, W. H., & Green, S. 1975, *ApJ*, 200, L175
- Gerin, M., Phillips, T. G., Benford, D. J., Young, K. H., Menten, K. M., Frye, B 1997, *ApJ*, 488, 31
- Goldreich, P. & Kwan, J. 1974, *ApJ*, 189, 441
- Green, S. 1991, *ApJS*, 76, 979
- Grundahl, F. & Hjorth, J. 1995, *MNRAS*, 275, L67
- Haar, D. ter & Pelling, M. A. 1974, *Rep. Prog. Phys.* 37, 481
- Henkel, C., Jethava, N., Kraus, A., Menten, K. M., Carilli, C. L., Grasshoff, M., Lubowich, D., & Reid, M. J. 2005, *A&A*, 440, 893
- Henkel, C., Walmsley, C. M., & Wilson, T. L. 1980, *A&A*, 82, 41
- Jethava, N., Henkel, C., Menten, K. M., Carilli, C. L., Reid, M. J., & Walmsley, C. M. 2007, *A&A*, 472, 435
- Kahane, C., Lucas, R., Frerking, M. A., Langer, W. D., & Encrenaz, P. 1984, *A&A*, 137, 211
- Kanekar, N., Chengalur, J. N., de Bruyn, A. G., & Narasimha, D. 2003, *MNRAS*, 345, L7
- Mangum, J. G., Darling, J., Menten, K. M., Henkel, C. 2008, *ApJ*, 637, 832
- Mengel, M., De Lucia, F. C. 2000, *ApJ*, 543, 271
- Menten, K. M. & Reid, M. J. 1996, *ApJ*, 465, L99
- Mittal, R., Procas, R., Wucknitz, O., Biggs, A., & Browne, I. 2006, *A&A*, 447, 515
- Mühle, S., Seaquist, E. R. & Henkel, C. 2007, *ApJ*, 671, 1579
- Muller, S., Guelin, M., Combes, F., & Wiklind, T. 2007, *A&A*, L468, 53
- O'Dea, C. P., Baum, S. A., Stanghellini, C., Dey, A., van Breugel, W., Deustua, S., & Smith, E. P. 1992, *AJ*, 104, 1320
- Palmer, P., Zuckerman, B., Buhl, D., & Snyder, L. E. 1969, *ApJ*, 156, L147
- Patnaik, A. R., Browne, I. W. A., King, L. J., Muxlow, T. W. B., Walsh, D., & Wilkinson, P. N. 1993, *MNRAS*, 261, 435
- Patnaik, A. R., Porcas, R. W., & Browne, I. W. A. 1995, *MNRAS*, 274, L5
- Pickett, H. M. et al. 1998, *J. Quant. Spectrosc., Radiat. Transfer* 60, 883
- Sobolev, V. V. 1960, *Moving Envelopes of Stars* (Cambridge, MA: Harvard Univ. Press)
- Solomon, P. M., Rivolo, A. R., Barrett, J., & Yahil, A. 1987, *ApJ*, 319, 730
- Townes, C. H. & Cheung, A. C. 1969, *ApJ*, 157, L103
- Wang, M., Henkel, C., Chin, Y.-N., Whiteoak, J. B., Hunt Cunningham, M., Mauersberger, R., & Muders, D. 2004, *A&A*, 422, 883.
- Wiklind, T. & Combes, F. 1995, *A&A*, 299, 382
- Wiklind, T. & Combes, F. 1999, *Highly Redshifted Radio Lines*, ASP Conf. Ser. 156, ed. C. L. Carilli, S. J. E. Radford, K. M. Menten, & G. I. Langston (San Francisco, CA: ASP) 202